EUROfusion

WPMST1-PR(18) 20275

N Walkden et al.

Fluctuation characteristics of the TCV snowflake divertor measured with high speed visible imaging

Preprint of Paper to be submitted for publication in
Plasma Physics and Controlled Fusion

This work has been carried out within the framework of the EUROfusion Consortium and has received funding from the Euratom research and training programme 2014-2018 under grant agreement No 633053. The views and opinions expressed herein do not necessarily reflect those of the European Commission.

This document is intended for publication in the open literature. It is made available on the clear understanding that it may not be further circulated and extracts or references may not be published prior to publication of the original when applicable, or without the consent of the Publications Officer, EUROfusion Programme Management Unit, Culham Science Centre, Abingdon, Oxon, OX14 3DB, UK or e-mail Publications.Officer@euro-fusion.org

Enquiries about Copyright and reproduction should be addressed to the Publications Officer, EUROfusion Programme Management Unit, Culham Science Centre, Abingdon, Oxon, OX14 3DB, UK or e-mail Publications.Officer@euro-fusion.org

The contents of this preprint and all other EUROfusion Preprints, Reports and Conference Papers are available to view online free at http://www.euro-fusionscipub.org. This site has full search facilities and e-mail alert options. In the JET specific papers the diagrams contained within the PDFs on this site are hyperlinked

Fluctuation characteristics of the TCV snowflake divertor measured with high speed visible imaging

N. R. Walkden[1], B. Labit[2], H. Reimerdes[2], J. Harrison[1], T. Farley[1,3], P. Innocente[4], F. Militello[1], the TCV Team‡ and the MST1 Team§
[1] **CCFE/UKAEA, Culham Science Centre, Abingdon, Oxfordshire, OX14 3DB, UK**
[2] **Swiss Plasma Center, Ecole Polytechnique Federale de Lausanne, Station 13, CH-1015, Lausanne, Switzerland**
[3] **Department of Electrical Engineering and Electronics, Univ. Liverpool, L69 3GJ, UK**
[4] **Consorzio RFX, Corso Stati Uniti, 4 - 35127, Padova, Italy**
Email: `nick.walkden@ukaea.uk`

Abstract. Tangentially viewing fast camera footage of the low-field side snowflake minus divertor in TCV is analysed across a four point scan in which the proximity of the two X-points is varied systematically. The apparent flow observed in the post-processed movie shows two distinct regions of the camera frame exhibiting differing flow patterns. One flow in the outer scrape-off layer remains present throughout the scan whilst the other, apparent in the inner scrape-off layer between the two nulls, becomes increasingly significant as the X-points contract towards one another. The spatial structure of the fluctuations in both regions is shown to conform to the equilibrium magnetic field. In all cases the primary X-point is quiescent. When the X-point gap is wide the fluctuations measured in the region between the X-points show a similar structure to the fluctuations observed above the null region, remaining coherent for multiple toroidal turns of the magnetic field and indicating a physical connectivity of the fluctuations between the upstream and downstream regions. When the X-point gap is small the fluctuations in the inner scrape-off layer between the nulls are decorrelated from fluctuations upstream, indicating local production of filamentary structures between the two nulls. The motion of filaments in the inter-null region differs, with filaments showing a dominantly poloidal motion along magnetic flux surfaces when the X-point gap is large, compared to a dominantly radial motion across flux-surfaces when the gap is small. This demonstrates an enhancement to cross-field tranport between the nulls of the TCV low-field-side snowflake minus when the gap between the nulls is small.

‡ See the author list of "S.Coda et al., Nucl. Fusion 57 (2017) 102011"
§ See the author list of "H.Meyer et al., Nucl. Fusion 57 (2017) 102014"

1. Introduction

Optimising divertor conditions for a tokamak based fusion reactor is a key area of research activity[1, 2, 3]. The high heat fluxes expected to impinge on the surface of the divertor target must be mitigated to ensure machine survival. This places a degree of importance on heat transport contributing to the profile of the heat flux to the material surface [4]. Likewise, particle transport has an important role in aspects of the machine operation including fuel retention, material migration, erosion and sputtering [5, 6]. Moreover, due to the challenging heat fluxes the standard operating scenario for ITER will likely include a partially detached divertor [7], which greatly reduces the heat flux to the divertor target. Detachment onset and detachment front control are very sensitive to both the electron temperature and the electron density along the divertor leg which in turn are sensitive to the transport processes within that region. Transport processes parallel to the magnetic field are routinely captured in two-dimensional fluid codes such as SOLPS [8], EDGE2D [9] or UEDGE [10] and may be considered reasonably well understood. Perpendicular transport processes on the other hand are generally rather poorly understood, and are usually captured heuristically in 2D fluid codes. Upstream, adjacent to the core plasma, perpendicular transport in the scrape-off layer is intermittent [11, 12, 13, 14, 15] and highly non-diffusive [16, 17]. A significant component of the heat and particles carried into and through the SOL perpendicular to the magnetic field is carried in intermittent coherent turbulent objects known as filaments/blobs [12, 18, 19]. These structures have been documented and analysed on many machines worldwide and are routinely modelled in both isolated filament simulations [20, 21, 22, 23, 24] as well as fully turbulent simulations. Filaments are also present below the X-point. Recent analysis of the MAST divertor region [25, 26, 27] showed a rather complex multi-region picture of cross-field transport. Turbulent structures appear in the far-SOL of the outer divertor leg, which connect to structures born upstream which flow down into the divertor volume via parallel transport. Filaments also appear in the private-flux region (PFR) which are born in the inner divertor leg [26], and in the near-separatrix region of the outer divertor leg. These divertor localised outer leg filaments exist with shorter lifetimes than elsewhere. Local to the X-point there are not detectable fluctuations when measured with tangential view high speed imaging, leading to the definition of the quiescent X-point region (QXR) [27]. The QXR conforms well to the magnetic flux-surfaces local to the X-point. The presence of the QXR indicates that the geometry of the null region can have a significant impact on the turbulent transport processes in the divertor volume that contribute to profile structures at the divertor surfaces.

To complement the conventional divertor design a suite of 'alternative' divertor concepts exist which exploit novel designs to optimize conditions at the divertor surface towards tolerable levels in a future tokamak based fusion reactor. One such advanced divertor concept is the 'snowflake' divertor [28, 29]. In the ideal snowflake divertor a second-order null in the poloidal magnetic field is achieved such that both the conditions $B_p = 0$

and $\nabla B_p = 0$ are satisfied [28]. This leads to a locally hexagonal structure in the poloidal field, with two limbs forming the separatrix that encircles the core plasma, whilst the other four connect to targets at the divertor forming the primary plasma-surface interface of the machine. The snowflake has a larger region of low poloidal magnetic field by virtue of its higher order null point compared to the standard divertor. This leads to strong flaring of the magnetic flux surfaces local to the null region which increases the plasma volume in the divertor available to radiate power [30]. A drastic increase in field-line connection length is also present which leads to enhanced power losses along the magnetic field-line compared to a conventional divertor.

In practice the ideal snowflake configuration is a single point in the operational space of the machine and requires unobtainable precision in the control system of the machine to maintain. Rather two alternate configurations, the snowflake minus (SF-) and snowflake plus (SF+), are formed by bringing two X-points into close proximity [31]. The primary route by which a reduced net power to the divertor target is achieved in the Snowflake divertor is by redistributing power and particles from upstream onto the two divertor legs that are not topologically connected to the upstream SOL [32]. This relies on cross-field transport in some fashion to provide a mechanism by which this redistribution can occur. As has been shown on MAST [27], the null region can impact the nature of turbulent cross-field transport and even inhibit it entirely. In the snowflake divertor however, the expanded region of low poloidal magnetic field has been predicted to give rise to a 'churning' mode providing plasma convection to the snowflake divertor legs that are not primarilly connected to the plasma core [33]. The presence of a second X-point in the outboard side SOL has been shown to impact upstream SOL profiles [34] leading to moderate increases in the near SOL density and electron temperature. This paper now seeks to provide a thorough characterisation of the properties of scrape-off layer fluctuations in snowflake plasmas with an X-point in the outer SOL.

In section 2 the setup of the fast camera and the experimental data used in this study are introduced. In section 3 the main results of the study are described. General properties of the fluctuations within the movie time-series are analysed, before a detail analysis of the spatial and temporal characteristics of fluctuations in different regions of the movie are carried out. Section 4 discusses the results and presents a hypothesis to describe the observed fluctuation behaviour as the X-point gap narrows and section 5 concludes.

2. Experimental Setup

The experiments studied here were performed on TCV [35] and comprise a four-point scan in the parameter ρ_{X2} which parameterises the distance between two X-points in the LFS SF- configuration. ρ_{X2}, as defined in ref [31], is given by

$$\rho_{X2} = \sqrt{\frac{\psi_{X2} - \psi_0}{\psi_{X1} - \psi_0}} \tag{1}$$

where ψ_{X2}, ψ_{X1} and ψ_0 are the poloidal magnetic flux at the secondary X-point, primary X-point and magnetic axis respectively such that ρ_{X2}^2 gives the normalised poloidal flux of the flux-surface that intersects the outer X-point. The two topological variants of the snowflake, the snowflake minus (SF-) and snowflake plus (SF+) are described by $\rho_{X2} > 1$ and $\rho_{X2} < 1$ respectively. In this contribution the low-field side (LFS) SF- configuration is studied, where the secondary X-point is situated in the LFS SOL. At $\rho_{X2} = 1.09$ the outer separatrix terminates on the outer wall and the X-points are strongly separated from one-another. At the opposite end of the scan, at $\rho_{X2} = 1.01$, the two separatrices are very close to one-another upstream and the X-points are in close proximity in the divertor. Figure 1 shows the magnetic configuration for the four plasmas in the ρ_{X2} scan. The strike points in the snowflake are labelled as SP1 to SP4

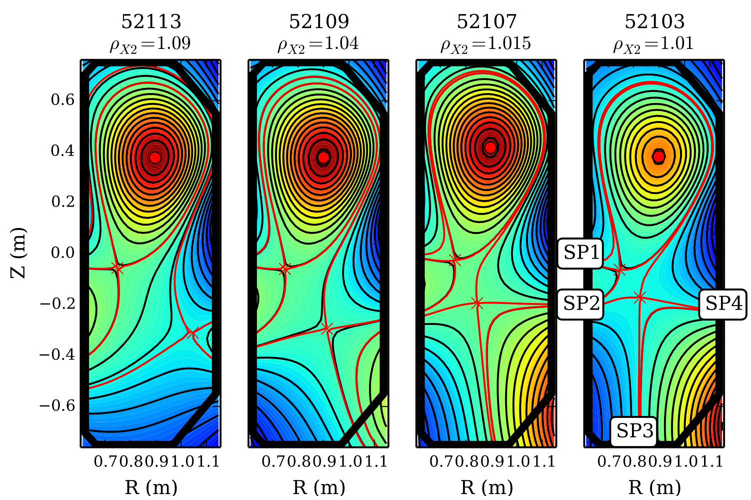

Figure 1. Magnetic equilibria in the four plasmas studied in this contribution representing a scan in the parameter ρ_{X2}, calculated at $t = 0.91$s. All equilibria are calculated at a time of 0.91s at a comparable density. The individual divertor leg strike points are labelled SP1 to SP4 with SP1 as the inner upper strike point and the labelling proceeding anti-clockwise. This is displayed for the case of 52103, and the convention is the same for all four. Color contours in this figure, as well as all other figures illustrating the magnetic equilibrium represent the variation of the poloidal magnetic flux.

sequentially, beginning at the inner-upper strike point and proceeding anti-clockwise. These have been labelled in figure 1 for plasma 52103, but the convention is the same for all four cases. The scan is conducted in Ohmic L-mode attached Deuterium plasmas with no external heating, with a slow fuelling ramp leading to a gradual increase in line-averaged density throughout the shot. Other than the proximity of the secondary X-point, all plasma parameters are comparable during the scan. Time windows for analysis are chosen such that the plasma density in each case is comparable and the plasmas are in an attached regime. Figure 2 shows the line-averaged density, plasma current and toroidal magnetic field evolution for the four equilibria in the ρ_{X2} scan.

The camera model used for analysis here is a Photron APX-RS and was operated at a frame-rate of 50kHz with an integration time of $20\mu s$ and a pixel-resolution of 128x176

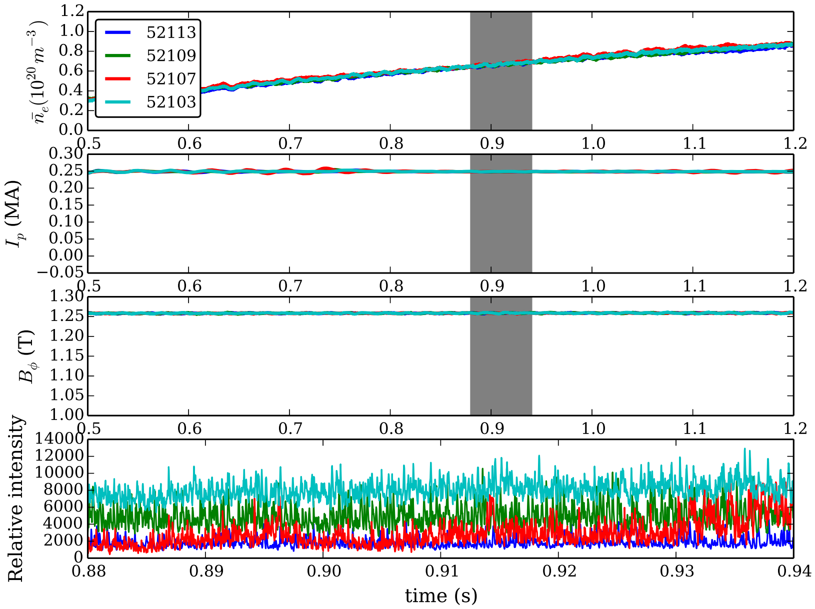

Figure 2. First three rows: Line-averaged density, plasma current and toroidal magnetic field for the four plasmas in the ρ_{X2} scan. The window within which analysis has been conducted is shaded in grey. Lowest row: Time-trace of the raw pixel intensity measured on a camera pixel that views the outer scrape-off layer.

in the horizontal and vertical dimension respectively. At the camera tangency angle this provides a spatial resolution of 5mm. The camera was mounted to a midplane viewing port on the TCV vessel and had a tangential line of sight towards the plasma, encompassing approximately a half-view of the interior. Figure 3 shows a rendering of the camera view into the TCV vessel, overlaid with a false color image from plasma 52103. The camera is unfiltered and sensitive to the visible spectrum meaning that any

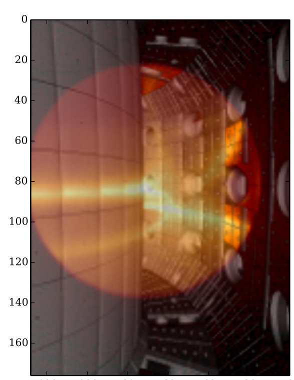

Figure 3. Rendering of the camera view into a CAD visualisation of the TCV vessel. Overlaid in a false heat-map is an image from 52103 to show the context of the camera view.

emission from the plasma at visible wavelengths contributes to the camera image. Since the intensity of the camera image is uncalibrated and the image is unfiltered no attempt has been made to characterise the spectral properties of the emission. Scrape-off layer fluctuations present in the camera image are likely to be caused primarily by fluctuations in the plasma conditions which can be inferred by their adherence to the structure of the background magnetic field. Also shown in the final row of figure 2 are typical time series of the raw intensity measured on a pixel of the camera sensor viewing the outboard SOL region of the plasma during the analysis time window. In each case the signal is observed to fluctuate strongly, similar to typical signals obtained on Langmuir probes. To isolate the fluctuating component of the movie a background subtraction technique has been applied where the pixel-wise minimum of the intensity of the frame of interest alongside the ten preceding frames is subtracted from the frame of interested. This removes the slow varying background emission and isolates only the rapidly fluctuating component of the light emission measured by the camera. The technique has been successfully applied to data from MAST for the analysis of fluctuations near the midplane [36, 37, 38] and in the divertor [25, 26, 27]. In figure 4 examples of movie frames from TCV plasma discharges 52113 and 52103 are shown before and after post-processing, demonstrating the effective isolation of the fluctuating component of the light.

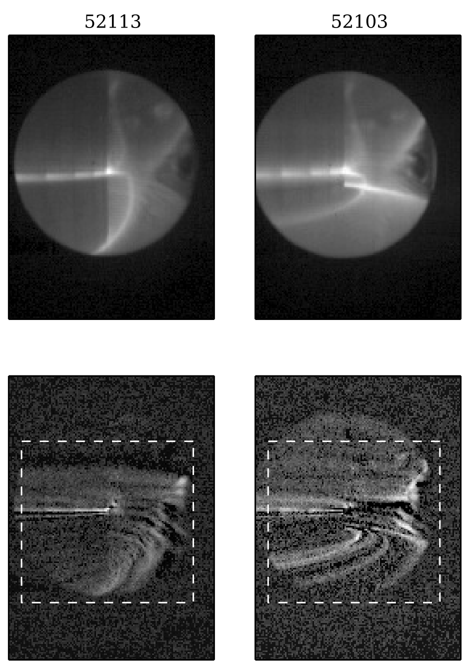

Figure 4. Example of the post-processed background subtraction used to extract the fluctuating component of the light picked up by the camera in plasmas 52113 and 52103. The same technique is applied to the other two plasmas in the scan. A gamma enhancement with $\gamma = 0.5$ has been applied to the images shown here for visual clarity, but is not used in the subsequent analysis. Since a significant proportion of the camera sensor is dark, a region of interest (ROI) has been chosen that encompasses the area of the movie where the null region is visible. This is the region inside the dashed box in the lower row.

The analysis conducted in the following sections is taken over a time-series of 3000 frames (60ms) in a time-range where the plasma conditions are relatively stationary and comparable between the different plasmas. The analysis window is highlighted with a shaded area in figure 2. A large time-series is required to ensure accuracy of the various statistical measures used in the forthcoming analysis. $60ms$ was found to provide a good balance between the need for stationary plasma conditions and statistical convergence of the measures used for analysis.

3. Results

In all cases within the scan of ρ_{X2} a strong fluctuating component of the light viewed by the camera is present in the SOL. The distribution of this fluctuating light in the camera image plane varies as the magnetic configuration is alterred. In figure 5 (upper row) the distribution of the pixel-wise standard deviation on the camera image plane is shown for all four plasmas in the ρ_{X2} scan. A rise in the standard deviation on a given pixel

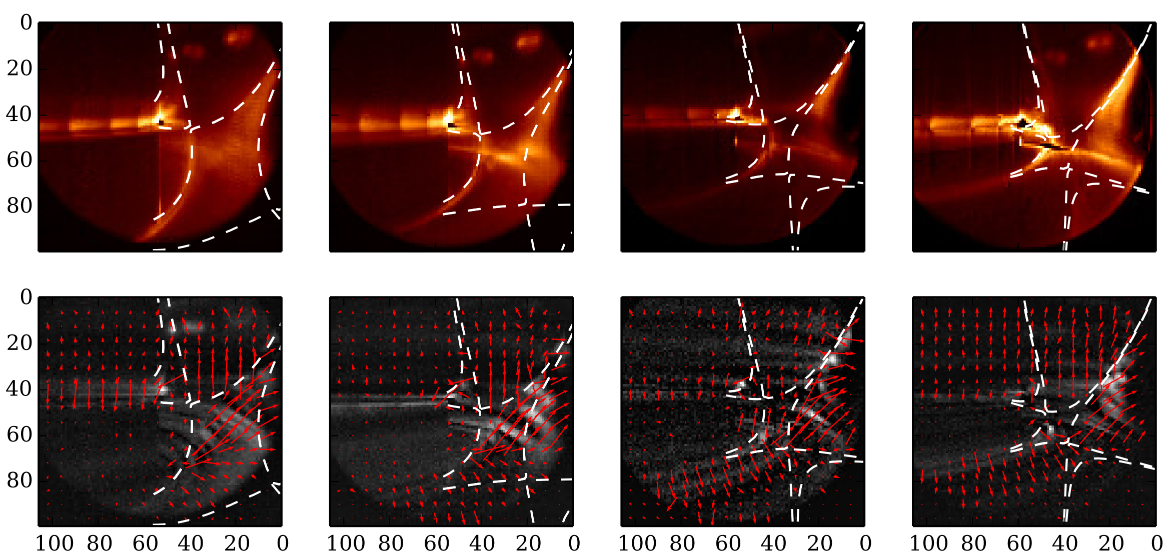

Figure 5. Upper: Pixel-wise fluctuation amplitude measured in the camera view for each plasma in the ρ_{X2} scan. Separatrices corresponding to the two X-point flux-surfaces are projected onto the image. Lower: Apparent flow on the camera image plane due to fluctuations in the image time-series overlaid on an image from the time-series.

can be interpreted as an indication of a significant fluctuating component of the light picked up by that pixel. The standard deviation naturally increases in regions where the camera sight line is near-tangent to the magnetic field, since in these line-integration is maximised. There is also a natural increase of the standard deviation in regions around the plasma-material interface, where local increases in the neutral density can lead to increased light emission. The standard deviation conforms well to the geometry of the scrape-off layer flux-surfaces in all four cases indicating that fluctuations observed in the movie can be associated with scrape-off layer fluctuations, commonly termed blobs or filaments [19]. There is a reduction in the standard deviation in the region tending towards the primary X-point in each case. This is similar to observations made on MAST [27] where the X-point was shown to be quiescent.

In figure 5 (lower row) the typical pattern of the apparent flow observed in each movie is shown (given by the direction and magnitude of the arrows within the quiver diagram). This flow pattern is extracted using a correlation analysis based on similar techniques employed in particle velocimetry. For each image pixel respectively, two cross-correlations are calculated between the pixel and its nearest neighbours in the horizontal and vertical direction with time-delays of a frame in the future and a frame in the past. To recover the rate of change of the cross-correlation, the difference in the correlations at a positive and negative time delay is calculated. The horizontal and vertical components of the flow are then obtained by taking the difference of this quantity between the horizontal and vertical nearest neighbour pixels respectively. The full flow vector is calculated from these two components. There are two distinct flow patterns apparent in figure 5. There is a flow that is diagonal on a bearing of roughly 45 degrees (clockwise from vertical) and can be seen in all four cases at the right hand side of the frame. This coinsides with the region where the standard deviation peaks in the outboard scrape-off layer and corresponds to fluctuations in the outer SOL emanating from the upstream scrape-off layer. The direction of the flow points poloidally, roughly parallel with the magnetic surfaces local to that region of the image. It should be noted that the apparent poloidal motion of this flow cannot be disambiguated since a true poloidal flow or a poloidal projection of a toroidal flow of a field-aligned structure will appear the same in the two-dimensional movie. Since there is no neutral beam heating in the plasmas measured however, it is likely that externally driven toroidal flows will be minimal. The observed poloidal flow points in the ion diamagnetic direction (noting that the x-axis is reversed in all figures from the camera image plane presented here) which is also the direction expected of the scrape-off layer ExB flow assuming the potential in the scrape-off layer is set by the sheath potential which increases towards the separatrix. This poloidal flow is present in all cases, though as ρ_{X2} decreases, the region where the poloidal flow is present becomes more isolated to the outer scrape-off layer (outside the secondary separatrix). There is a second flow that becomes more prevalent as ρ_{X2} decreases and exists in the region between the two nulls. The flow has a bearing that varies between roughly 100 and 170 degrees at differing points in the image plane and crosses magnetic flux surfaces, indicating that it contributes to cross-field transport. The increased prevalence of this radial flow as ρ_{X2} increases implies that the additional null in the SF LFS- configuration impacts the properties of turbulent transport in the scrape-off layer.

The analysis presented so far indicates two regions where a deeper analysis of the fluctuation characteristics may be of importance. The two regions will be term the OSOL (Outer scrape-off layer) and ISOL (Inner scrape-off layer) and correspond to the regions in which the two different flow patterns become apparent. The OSOL here will be taken to as an outer region of the SOL above the X-points close to the secondary separatrix where the strong poloidal flow is apparent. The ISOL will be taken as a region below the primary X-point close to the inner separatrix linking to SP2 where the stronger radial motion is apparent. Note that these regions refer to areas in the movie frame and, whilst they do also correspond to similar regions in the poloidal plane, the aim here is to simply allow easy distinction between the two areas to be analysed. In addition to the ISOL and OSOL regions, the region close to the primary X-point will also be studied in some detail to investigate whether the quiescence observed in figure 5 is borne out in a deeper analysis of the fluctuation structures observed.

3.1. Spatial characteristics of the fluctuations

In this section the spatial structure of fluctuations in each of the three analysis regions will be investigated. The analysis proceeds by taking a representative pixel from each region and calculating the instantaneous cross-correlation of the data on that pixel with all other pixels within the frame over the time-series. Through this method the typical structure in the image frame of a fluctuation that crosses the selected pixel is obtained. This method has been used for similar purposes in the MAST divertor [27] where also the method was validated on synthetic data. Regions in the image showing a correlation of less that 15% with the selected pixel are set to zero in order to isolate the structure of the fluctuations under study.
In figure 6 shows the cross-correlation carried out in the OSOL, ISOL and X-Point regions of the image for each of the four plasmas in the ρ_{X2} scan. Each region will now be analysed in turn:

3.1.1. OSOL In the OSOL region the shape of the cross-correlation in the local vicinity of the selected pixel is similar in all four cases. This area is close the point where fluctuations that align with magnetic field-lines lie almost tangent to the camera LOS and so the emission that is captured primarily represents the cross-section of the fluctuation. In all four cases the fluctuations have a tendency towards an elliptically shaped cross-section with the dimension normal to the flux-surface larger than the dimension parallel to the flux surface. The ellipticity of the cross-section increases as ρ_{X2} decreases, as might be expected from the increase in flux expansion approaching the null region when ρ_{X2} is low. The elliptically shaped cross-section is consistent with these filaments originating further upstream and distorting in shape by following the topology of the magnetic field [39, 23, 40]. Furthermore each case shows regions of heightened correlation that are not directly connected to the selected pixel. This indicates a physical connectivity between the structure that overlaps the selected pixel and disconnected areas of the camera image plane. The most likely cause is alignment of the fluctuating structures to the background magnetic field. This can be demonstrated by projecting the trajectory of magnetic field-lines onto the camera image plane via a registration of the camera position using the `calcam` code ‖. In figure 7 magnetic

‖ Available at https://github.com/euratom-software/calcam

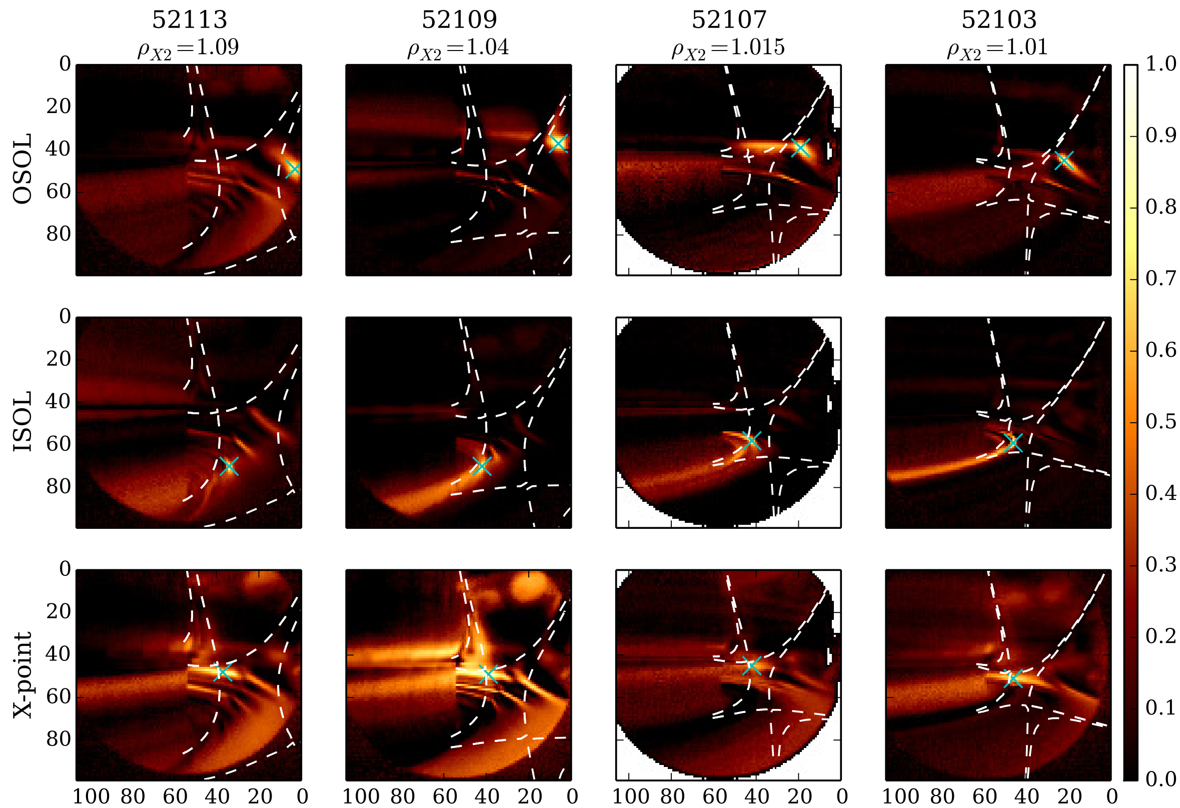

Figure 6. Cross-correlation analysis carried out for each plasma in the scan of ρ_{X2} with representative pixels from the OSOL region (upper row), the ISOL region (middle row) and the X-point region (lower row).

field-lines have been projected on the OSOL cross-correlation image that pass through the regions of high correlation for the two cases at the extreme ends of the ρ_{X2} scan.

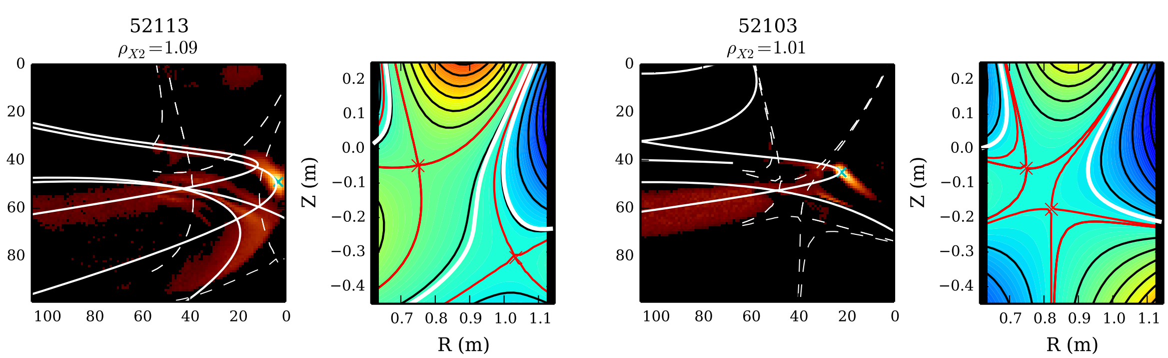

Figure 7. Magnetic field-lines projected onto the camera field of view that overlay the structures exhibited in the OSOL region of plasmas 52113 and 52103, the extrema of the ρ_{X2} scan. Also shown are the corresponding magnetic flux surfaces that the projected field-lines lie on. This analysis is carried out qualitatively since no good metric has been found to assess the quality of the projected field-line. For 52113, two magnetic field-lines have been chosen which intersect the correlation region surrounding the second pixel inside and outside the second separatrix respectively.

The cross-correlation structure shown in the OSOL is consistent with filamentary fluctuations maintaining a coherent structure along the magnetic field-line. Notably the structures in 52113 straddle the secondary separatrix, indicating that filaments from upstream are able to connect all the way through to SP2. This has been shown by projecting two magnetic field-lines that intersect the region of heightened correlation surrounding the selected pixel both inside and outside of the second separatrix. With both field-lines plotted, the correlation is relatively well mapped out. In the smaller ρ_{x2} cases the correlation appears confined to the outer SOL connecting to SP4 and a second field-line inside the secondary separatrix is not required to describe the shape of the correlation.

3.1.2. ISOL In the ISOL region a distinctly different behaviour is apparent as ρ_{X2} decreases. At large ρ_{X2} the structure of the correlation in figure 6 in the ISOL is similar to the structure found by selecting a pixel in the OSOL region. It shows multiple regions of correlation corresponding to the fluctuation connecting along the magnetic field both upstream and towards the divertor, with an elliptically shaped cross-section. Since similar structures are evident whether a pixel is selected in the OSOL or ISOL region at large ρ_{X2} it may be concluded that there is a true physical connection between the two regions. As in the OSOL case, this can be confirmed by projecting magnetic field-lines onto the correlation images. This is done for the two extreme cases of the scan in ρ_{X2} in figure 8.

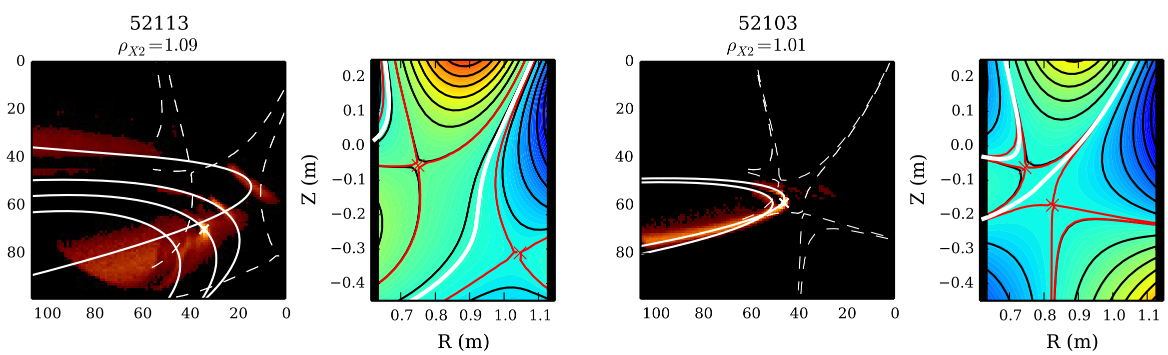

Figure 8. Similarly to figure 7, magnetic field lines are projected such that they overlay regions of high correlation in the ISOL region.

At large ρ_{X2} the correlation follows the trajectory of a magnetic field-line well in both the direction upstream and downstream, indicating a connectivity of the filamentary structures between the upstream and downstram regions along the magnetic field line connecting to SP2. This is not apparent in the smaller ρ_{X2} cases. At small ρ_{X2} the filamentary structure does not correlate for more than a maximum of two turns around the machine, and does not correlate with the upstream plasma. In the inter-null region the poloidal field is low and the field-line wraps tightly around the machine. Despite this, the poloidal deviation of the fieldline after one turn of the machine is still significant enough that, were the filament to connect further upstream, it should be expected to be distinguishable. Furthermore the cross-sectional shape of the fluctuations in the small ρ_{X2} case appear qualitatively less elliptical in the ISOL than the OSOL. Since the topological distortions of the filament cross-section due to the magnetic field should increase with proximity to the separatrix, if ISOL filaments originated upstream their cross-sections should be highly sheared. Since this is not the case, and since the correlation appears to be confined to the divertor region the evidence gathered here suggests that at small ρ_{X2} filaments are generated locally in the region between the two nulls in the TCV LFS SF- configuration.

3.1.3. X-Point Figure 5 suggests that the primary X-point region in all four cases within the scan of ρ_{X2} remains quiescent in the manner observed on MAST [27]. Despite this apparent quiescence, the correlation analysis produces rather complex structures when a pixel is selected close to the inner X-point. To elucidate the nature of these structures, once again magnetic field-lines have been projected onto the correlation images for the two extreme cases in the ρ_{X2} scan, shown in figure 9.

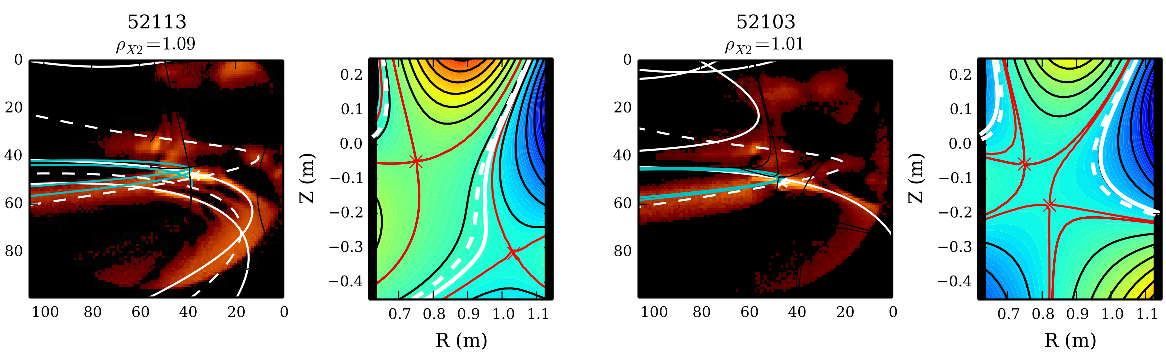

Figure 9. Similarly to figure 7 and 8, magnetic field lines are projected such that they overlay regions of high correlation in the region local to the inner X-point. In each case two separate magnetic field-lines are required to fully characterise the structure. These are represented by solid and broken white lines respectively. Cyan lines represent a projection of a magnetic fieldline situated close to the X-point twice around the machine.

In both cases two magnetic field-lines have been identified (one as a solid line and the other as a broken line) which map onto the regions of high correlation. The field lines both lie on flux-surfaces that are a significant distance into the SOL, away from the primary separatrix which intersects the primary X-point. This shows that the structures present can be described as filaments in the OSOL region that cross the X-point region in the image frame due to the projection of their toroidal structure onto the camera view. These structures are not located near the X-point in the poloidal plane but provide a source of emission that crosses the pixel selected in the X-point region in the image frame. Since the correlation structures local to the X-point region can be fully explained by these filaments that exist far from the X-point in the poloidal plane, it can be concluded that, as with the MAST analysis, the inner X-point of the TCV LFS SF- configuration is quiescent when measured with the tangential viewing unfiltered fast-camera at all values of ρ_{X2} investigated. For comparison, fieldlines that are in close proximity to the X-point have been projected onto the camera view (cyan lines in figure 9). Being close to the null, these fieldlines wrap very tightly around the machine. Whilst they may partially align with the correlation structure as they wrap around towards the camera, in front of the centre column, they cannot explain the complex structure of the correlation elsewhere. This, coupled with the observation from figure 5 that the apparently flow drops in the vicinity of the primary X-point, supports the assertion that the primary X-point appears quiescent. It is also worth noting that in 52113 the QXR terminates in the SOL well inside of the secondary separatrix, indicating that the presence of the QXR is not reliant on the presence of the secondary null point. This suggests that single null plasmas in TCV should be expected to show similar behaviour around the X-point.

3.2. Temporal characteristics of the fluctuations

The spatial structure of fluctuations in the three regions defined in the previous section, OSOL, ISOL and XP, were shown to vary as ρ_{X2} varied. The observation that, as ρ_{X2} decreases, filaments in the ISOL region become de-correlated from upstream, may also indicate that their motion will vary in comparison to the OSOL region. To investigate the temporal characteristics of the fluctuations a time delay can be introduced into the correlation. As a general quantifier of the temporal characteristics of fluctuations, the pixel-wise auto-correlation has been calculated at a time-lag of two frames. This can be interpreted as showing how strongly decorrelated a pixel becomes two frames after a fluctuation is present. Carrying this out for each pixel in the camera view shows regions of the image where pixels become decorrelated more quickly, indicating more rapid fluctuations. Figure 10 shows this time-lagged pixel-wise autocorrelation at $\rho_{X2} = 1.09$ and $\rho_{X2} = 1.01$ respectively. Also shown is the autocorrelation function for both cases sampled in the OSOL and ISOL respectively.

The region that has been associated with the localised ISOL filaments at smaller ρ_{X2} shows a pronounced reduction in the time-lagged autocorrelation compared with the OSOL region and with both regions at larger ρ_{X2}. In the ISOL the autocorrelation function contracts as ρ_{X2} decreases. This indicates that fluctuations in the ISOL region at small ρ_{X2} may evolve faster than their counterparts in the OSOL. Changes to the temporal properties of the filaments in the ISOL as ρ_{X2} decreases may indicate changes in their propagation and consequently changes to the transport that can be associated with them. The motion of fluctuations in the ISOL can be tracked by introducing a time delay into the cross-correlation analysis introduced in section 3.1. At a positive (negative) time-delay, the cross-correlation presents the typical structure found on the camera in the future (past) after a fluctuation is measured on the selected pixel. In this case time-delays are introduced stretching from two frames in the past to two frames in

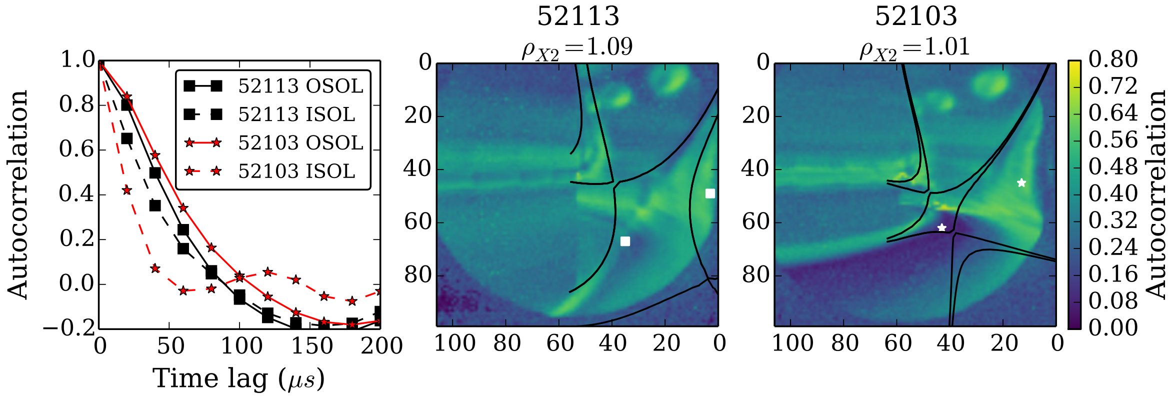

Figure 10. Left: Autocorrelation function in the ISOL and OSOL (positions marked on central and right hand figures) for plasmas 52103 and 52113 respectively. Centre and right: Pixel-wise autocorrelation calculated at a time-lag of two frames ($40\mu s$) for the image time-series in 52113 and 52103.

the future, giving a total window of $80\mu s$. Magnetic field-line projections are again used to infer the spatial structure of the cross-correlation, however this time two magnetic field-lines are projected that qualitatively bound the region of heightened correlation. The flux-surfaces that these magnetic field-lines lie on, as well as their position in the poloidal plane at the camera tangency angle, are shown in figure 11.

In both cases the ISOL fluctuations evolve in the inter-null region, however the details of their propagation differ. In 52103 the motion is mainly in the radial direction and the region of heightened correlation expands radially. By contrast in 52113 the radial motion and radial expansion is suppressed compared to 52103. There is a slightly more pronounced vertical motion in 52113, though this is difficult to distinguish visually. A more quantitative comparison is given in figure 12 where the poloidal plane trajectories of the structures in figure 11 are shown as a function of time.

Figure 12 shows a moderately faster radial motion in 52103 compared to 52113, but a reduced vertical motion. When mapped into the normalised poloidal flux (ψ_N) the difference between the two types of motion becomes clear. In 52103, where $\rho_{X2} = 1.01$ and the nulls are close, the motion is predominately across the magnetic field such the the fluctuations move outwards in ψ_N towards the secondary separatrix. By contrast the motion observed in 52113 remains approximately stationary in ψ_N indicating a predominantly poloidal flow. It can therefore be concluded that as the nulls of the TCV LFS SF- contract towards smaller ρ_{X2} isolated fluctuations in the inter-null region start to develop which provide a intermittent cross-field flux that enhances transport between the nulls.

4. Discussion

The main observation made here is that as ρ_{X2} decreases in the LFS SF- configuration radial transport, mediated by intermittent filamentary fluctuations, increases in the

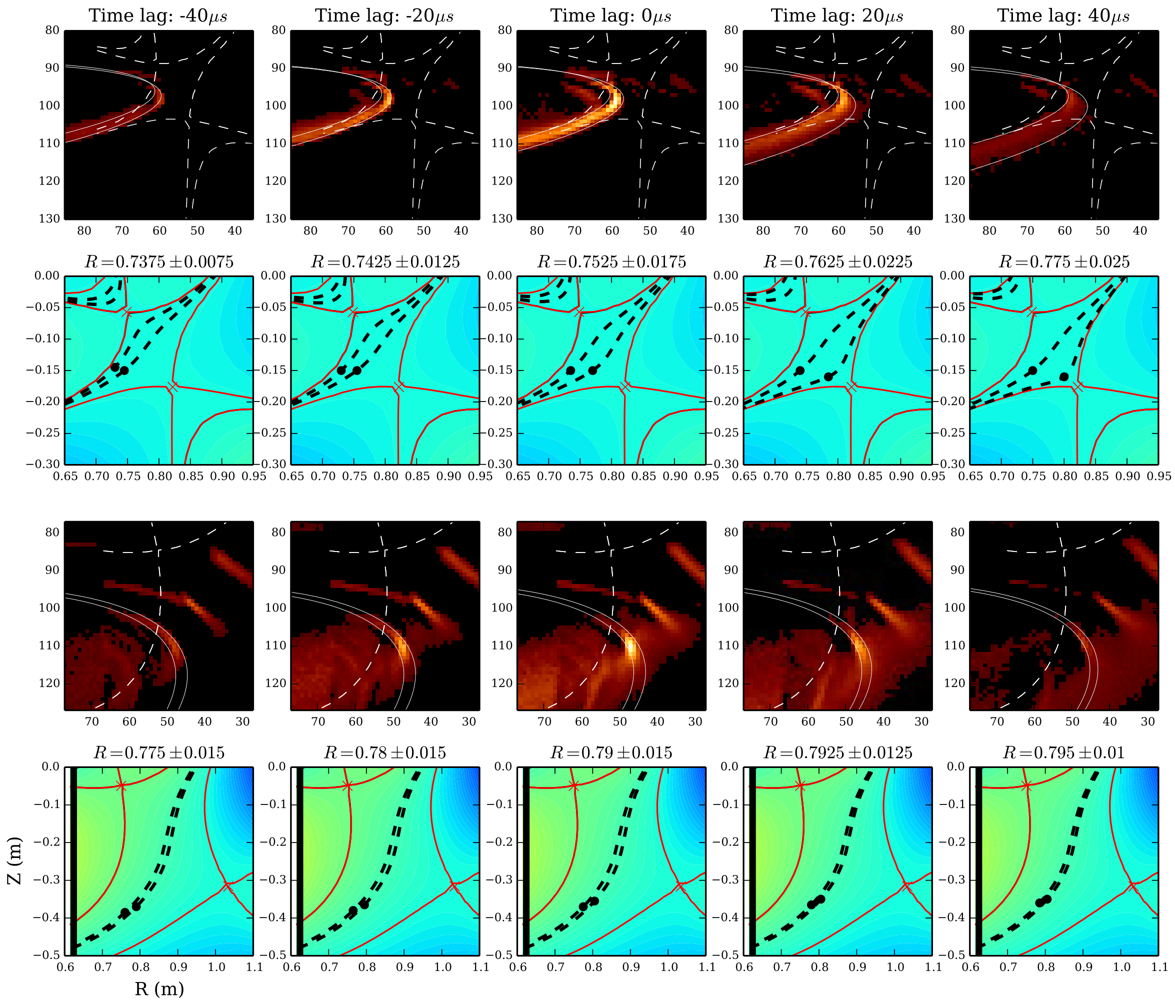

Figure 11. Time-delayed cross-correlation in the ISOL regio stretching from a delay of two frames in the past to two frames in the future. Magnetic field lines have been projected which qualitatively encompasses the region of heightened correlation. This region is tracked through the series. Magnetic flux surfaces are indicated with dashed lines and positions in the poloidal plane at the camera tangency angle, indicated as closed circles, of the two magnetic field-lines projected in the camera image. The upper two rows correspond to plasma 52103 ($\rho_{X2} = 1.01$) whilst the lower two rows correspond to plasma 52113 ($\rho_{X2} = 1.09$).

region between the two null points due to the localised production of filaments that propagate radially between the nulls. This observation is supported by recent measurements on TCV using both infra-red and probe diagnostics that show an enhanced level of transport resulting in broader profiles between the nulls of the TCV LFS SF- configuration compared to the single-null case [41]. The LFS SF- configuration has also been shown to support a radiation front away from the primary X-point in the inter-null region in conditions where the single-null case radiates from the X-point and inner divertor leg [30]. It is possible that enhanced filamentary transport in the inter-null region may play a role in broadening profiles within the null region and helping to

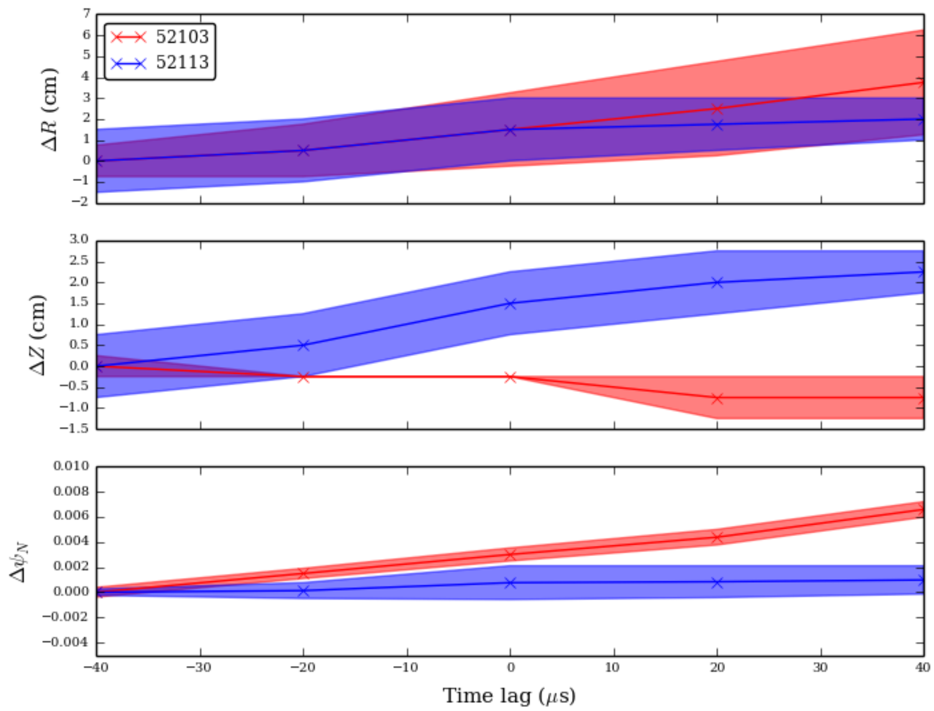

Figure 12. Radial (upper), vertical (middle) and normalised poloidal flux (lower) trajectories of the ISOL structures in tracked in figure 11 in the poloidal plane. The shaded region corresponds to the region enclosed by the field-lines used to track the structures in figure 11. Red curves correspond to plasma 52103 whilst blue curves correspond to 52113.

move the radiation front away from primary null. This paper has also demonstrated the presence of a quiescent region near the primary X-point (QXR), a phenomenon first observed in MAST. The interplay between the QXR and the fluctuations observed in the OSOL and ISOL is difficult to determine from the camera footage, though it may be notable that the ISOL localised fluctuations appear most strongly when the secondary X-point lies on a flux that coinsides with the QXR. It is likely that detailed non-linear numerical simulation will be required before the underlying physical mechanisms governing the OSOL and ISOL fluctuations and the QXR can be understood.

One notable difference between the fluctuations in the large and small ρ_{X2} cases is the the connectivity of filaments along magnetic field-lines. In particular the ISOL localised filaments observed in the small ρ_{X2} case appear to correlate strongly at most twice toroidally along the magnetic field. In the ISOL region the poloidal magnetic field is substantially reduced by virtue of the proximity to the nulls, and therefore the magnetic field followed by the filaments is dominantly toroidal (more so than in the outer region of the SOL, or in the case when ρ_{X2} is large). In this scenario a model was proposed by Ricci and Rogers [42] following measurements on TORPEX [43] whereby a filament at its development phase is able to overlap itself and consequently short-circuits the current paths that determine its motion. It is not clear whether this model is consistent with filaments in the SF LFS- ISOL, however given that these filaments appear to form in a region of much lower poloidal magnetic field than their upstream counterparts, it is reasonable to consider whether differing mechanisms for current closure may apply. In addition filament motion in the vicinity of an X-point has been studied on TORPEX [44] and numerically [45] which suggested that background flows in the vicinity of the X-point may affect the trajectory of filaments.

This study has only considered the SF LFS- configuration, however as discussed in the introduction and in refs [31, 32], other topological forms of the snowflake divertor exist. In the SF+ configuration the second X-point lies in the private-flux region of the first, meaning that it cannot lie within the QXR of the outboard SOL. Likewise in the HFS SF- configuration the second X-point lies within the inboard SOL, so once again does not overlap with the QXR in the outboard SOL. It is unclear how the results of this study transfer to these other two configurations and this should be pursued to provide a fuller understanding both of the fluctuation characteristics of snowflake divertors and the role played by the null region on turbulent fluctuations. A study of the density dependance of the ISOL and OSOL fluctuations would also be a good avenue of future work.

5. Conclusions

This contribution analyses fast visibile imaging footage from a tangentially viewing unfiltered camera of the null region in the TCV low-field side snowflake minus (LFS SF-) configuration. Four plasmas are compared that comprise a scan in the quantity ρ_{X2} which parameterises the distance (in normalised flux) between the two X-points of the LFS SF- configuration. As ρ_{X2} decreases and the X-point gap contracts the fluctuation amplitude picked up by the camera becomes increasingly peaked in the outboard SOL region. In addition two apparent distinguishable flows are shown to be present in the movies. The first corresponds to a poloidal flow of fluctuations in the outer SOL region (OSOL) and is prominent in all plasmas. The second corresponds to a radial motion in the inner SOL (ISOL) region between the two null points and becomes increasingly prominent as the X-points contract towards one another. Based on this observation, a cross-correlation technique was used to analyse the spatial structure of fluctuations in both the OSOL and ISOL regions, as well as locally around the X-point. The primary X-point is shown to be quiescent, consistent with a previous study of the X-point region of MAST. At larger ρ_{X2} fluctuations are observed to connect along magnetic field-lines between upstream and downstream, into the ISOL region. At smaller ρ_{X2} fluctuations in the divertor are uncorrelated with upstream, indicating a local production of turbulent structures between the two nulls of the LFS SF-. The typical motion of the ISOL structures is tracked and a distinct difference in the motion of filaments at large and small ρ_{X2} is shown. At large ρ_{X2} filaments in the ISOL region move predominantly in the poloidal direction along flux-surfaces. By contrast at small ρ_{X2} ISOL filaments move mainly in the radial direction across flux-surfaces, indicating an enhancement to cross-field transport between the two nulls of the TCV LFS SF- configuration when ρ_{X2}

is small.

6. Acknowledgements

This work has been carried out within the framework of the EUROfusion Consortium and has received funding from the Euratom research and training programme 2014-2018 under grant agreement No 633053. The views and opinions expressed herein do not necessarily reflect those of the European Commission.

7. References

[1] A. Loarte *et al.*, Nuclear Fusion **47**, S203 (2007).
[2] B. Lipschultz *et al.*, Nuclear Fusion **47**, 1189 (2007).
[3] R.Wenninger *et al.*, Nuclear Fusion **55**, 063003 (2015).
[4] T. Eich *et al.*, Physical Review Letters **107**, 215001 (2011).
[5] S.Brezinsek *et al.*, Nuclear Fusion **55**, 063021 (2015).
[6] R.Behrisch, G.Federici, A.Kukushkin, and D.Reiter, Journal of Nuclear Materials **313**, 388 (2003).
[7] T.Eich *et al.*, Nuclear Fusion **53**, 093031 (2013).
[8] R.Schneider *et al.*, Contributions to Plasma Physics **46.1-2**, 3 (2006).
[9] G.J.Radford *et al.*, Contributions to Plasma Physics **36**, 187 (1996).
[10] T.Rognlien, J.L.Milovich, M.E.Rensink, and G.D.Porter, Journal of Nuclear Materials **196-198**, 347 (1992).
[11] G. Y. Antar *et al.*, Physics of Plasmas **10**, 419 (2003).
[12] J. A. Boedo *et al.*, Physics of Plasmas **10**, 1670 (2003).
[13] O.E.Garcia *et al.*, Nuclear Fusion **47**, 667 (2007).
[14] B. D. Dudson *et al.*, Plasma Physics and Controlled Fusion **47**, 885 (2005).
[15] G. S. Xu *et al.*, Nuclear Fusion **49**, (2009).
[16] V. Naulin, Journal of Nuclear Materials **363–365**, 24 (2007).
[17] O. E. Garcia *et al.*, Journal of Nuclear Materials **363-365**, 575 (2007).
[18] S. I. Krashenninikov, Physics Letters A **283**, 368 (2001).
[19] D. A. D'Ippolito, J. R. Myra, and S. J. Zweben, Physics of Plasmas **18**, 060501 (2011).
[20] G.Q.Yu and S.I.Krasheninnikov, Physics of Plasmas **10**, 4413 (2003).
[21] O. E. Garcia *et al.*, Plasma Physics and Controlled Fusion **48**, L1 (2006).
[22] G. Q. Yu, S. I. Krasheninnikov, and P. N. Guzdar, Physics of Plasmas **13**, 042508 (2006).
[23] N. R. Walkden, B. D. Dudson, and G. Fishpool, Plasma Physics and Controlled Fusion **55**, 105005 (2013).
[24] L. Easy *et al.*, Physics of Plasmas **21**, 122515 (2014).
[25] J.R.Harrison, G.M.Fishpool, and B.D.Dudson, Journal of Nuclear Materials **463**, 757 (2015).
[26] J.R.Harrison *et al.*, Physics of Plasmas **22**, 092508 (2015).
[27] N.R.Walkden *et al.*, Nuclear Fusion **57**, 126028 (2017).
[28] D. D. Ryutov, Physics of Plasmas **14**, 064502 (2007).
[29] F.Piras *et al.*, Plasma Physics and Controlled Fusion **51**, 055009 (2009).
[30] H.Reimerdes *et al.*, Nuclear Fusion **57**, 126007 (2017).
[31] B.Labit *et al.*, Nuclear Materials and Energy **12**, 1015 (2017).
[32] W.A.J.Vijvers *et al.*, Nuclear Fusion **54**, 023009 (2014).
[33] D.D.Ryutov *et al.*, Phys. Scr. **89**, 088002 (2014).
[34] C.Tsui *et al.*, 58th Annual Meeting of the APS devision of Plasma Physics, San Jose, CA (2016).
[35] S.Coda *et al.*, Nuclear Fusion **55**, 10 (2015).
[36] N. B. Ayed *et al.*, Plasma Physics and Controlled Fusion **51**, 035016 (2009).

[37] B. D. Dudson *et al.*, Plasma Physics and Controlled Fusion **50**, 124012 (2008).
[38] A.Kirk *et al.*, Plasma Physics and Controlled Fusion **58**, 085008 (2016).
[39] D. Farina, R. Pozzoli, and D. D. Ryutov, Nuclear Fusion **33**, 1315 (1993).
[40] N.R.Walkden, *Properties of intermittent transport in the Mega Ampere Spherical Tokamak* (PhD Thesis, University of York, 2014).
[41] R.Maurizio, Private communication. Results to be published in Nucl. Fusion (2018).
[42] P.Ricci and B.N.Rogers, Physical Review Letters **104**, 145001 (2010).
[43] S.H.Muller *et al.*, Plasma Physics and Controlled Fusion **51**, 055020 (2009).
[44] F.Avino *et al.*, Physical Review Letters **116**, 105001 (2016).
[45] B.W.Shanahan and B.D.Dudson, Plasma Physics and Controlled Fusion **58**, 125003 (2016).